2015

Fiber-optic refractometer based on a phase-shifted fiber Bragg grating on a side-hole fiber

Qi Zhang

Lingling Hu

Yuefeng Qi

G. Liu

Natale J. Ianno

See next page for additional authors

Authors
Qi Zhang, Lingling Hu, Yuefeng Qi, G. Liu, Natale J. Ianno, and Ming Han

Fiber-optic refractometer based on a phase-shifted fiber Bragg grating on a side-hole fiber

Qi Zhang,[1] Lingling Hu,[1] Yuefeng Qi,[1,2] Guigen Liu,[1] Natale Ianno,[1] and Ming Han[1,*]

[1]*Department of Electrical and Computer Engineering, University of Nebraska-Lincoln, 844 N. 16th St., Lincoln, Nebraska 68588, USA*

[2]*College of Information Science and Engineering, Yanshan University, Qinhuangdao, Hebei Province 066004, China*

**mhan3@unl.edu*

Abstract: A fiber-optic refractive index (RI) sensor based on a π-phase-shifted fiber-Bragg-grating (πFBG) inscribed on a side-hole fiber is presented. The reflection spectrum of the πFBG features two narrow notches associated with the two polarization modes and the spectral spacing of the notches is used for high-sensitivity RI sensing with little temperature cross-sensitivity. The side-hole fiber maintains its outer diameter and mechanical strength. The side-hole fiber is also naturally integrated into a microfluidic system for convenient sample delivery and reduced sample amount. A novel demodulation method based on laser frequency modulation to enhance the sensor dynamic range is proposed and demonstrated.

OCIS codes: (060.2370) Fiber optics sensors; (060.3735) Fiber Bragg gratings; (060.2630) Frequency modulation; (060.4005) Microstructured fibers.

References and links

1. A. Asseh, S. Sandgren, H. Ahlfeldt, B. Sahlgren, R. Stubbe, and G. Edwall, "Fiber optical Bragg grating refractometer," Fiber Integr. Opt. **17**(1), 51–62 (1998).
2. A. N. Chryssis, S. M. Lee, S. B. Lee, S. S. Saini, and M. Dagenais, "High sensitivity evanescent field fiber Bragg grating sensor," IEEE Photon. Technol. Lett. **17**(6), 1253–1255 (2005).
3. X. Fang, C. R. Liao, and D. N. Wang, "Femtosecond laser fabricated fiber Bragg grating in microfiber for refractive index sensing," Opt. Lett. **35**(7), 1007–1009 (2010).
4. O. Frazão, T. Martynkien, J. M. Baptista, J. L. Santos, W. Urbanczyk, and J. Wojcik, "Optical refractometer based on a birefringent Bragg grating written in an H-shaped fiber," Opt. Lett. **34**(1), 76–78 (2009).
5. M. Han, F. Guo, and Y. Lu, "Optical fiber refractometer based on cladding-mode Bragg grating," Opt. Lett. **35**(3), 399–401 (2010).
6. A. Iadicicco, A. Cusano, A. Cutolo, R. Bernini, and M. Giordano, "Thinned fiber Bragg gratings as high sensitivity refractive index sensor," IEEE Photon. Technol. Lett. **16**(4), 1149–1151 (2004).
7. H. Y. Meng, W. Shen, G. B. Zhang, C. H. Tan, and X. G. Huang, "Fiber Bragg grating-based fiber sensor for simultaneous measurement of refractive index and temperature," Sens. Actuators, B **150**(1), 226–229 (2010).
8. Y. Ran, Y. N. Tan, L. P. Sun, S. Gao, J. Li, L. Jin, and B. O. Guan, "193 nm excimer laser inscribed Bragg gratings in microfibers for refractive index sensing," Opt. Express **19**(19), 18577–18583 (2011).
9. J. Li, H. Wang, L. P. Sun, Y. Huang, L. Jin, and B. O. Guan, "Etching Bragg gratings in Panda fibers for the temperature-independent refractive index sensing," Opt. Express **22**(26), 31917–31923 (2014).
10. Y. Ran, L. Jin, L. P. Sun, J. Li, and B. O. Guan, "Bragg gratings in rectangular microfiber for temperature independent refractive index sensing," Opt. Lett. **37**(13), 2649–2651 (2012).
11. A. Othonos and K. Kalli, *Fiber Bragg Gratings: Fundamentals and Applications in Telecommunications and Sensing* (Artech House, 1999).
12. K. O. A. U. C. Paek, *Silica Optical Fiber Technology for Devices and Components: Design, Fabrication, and International Standards* (John Wiley & Sons, 2012).
13. H. Henschel, S. K. Hoeffgen, J. Kuhnhenn, and U. Weinand, "Influence of manufacturing parameters and temperature on the radiation sensitivity of fiber Bragg gratings," IEEE Trans. Nucl. Sci. **57**(4), 2029–2034 (2010).
14. Q. Zhang, N. Liu, T. Fink, H. Li, W. Peng, and M. Han, "Fiber-optic pressure sensor based on pi-phase-shifted fiber Bragg grating on side-hole fiber," IEEE Photon. Technol. Lett. **24**(17), 1519–1522 (2012).
15. J. Tian, Q. Zhang, T. Fink, H. Li, W. Peng, and M. Han, "Tuning operating point of extrinsic Fabry-Perot interferometric fiber-optic sensors using microstructured fiber and gas pressure," Opt. Lett. **37**(22), 4672–4674 (2012).

#238231 Received 16 Apr 2015; revised 4 Jun 2015; accepted 14 Jun 2015; published 17 Jun 2015

16. N. Zhong, Q. Liao, X. Zhu, Y. Wang, and R. Chen, "High-quality fiber fabrication in buffered hydrofluoric acid solution with ultrasonic agitation," Appl. Opt. **52**(7), 1432–1440 (2013).
17. Q. Zhang, N. J. Ianno, and M. Han, "Fiber-optic refractometer based on an etched high-Q π-phase-shifted fiber-Bragg-grating," Sensors (Basel) **13**(7), 8827–8834 (2013).
18. Q. L. Ma, T. Rossmann, and Z. X. Guo, "Whispering-gallery mode silica microsensors for cryogenic to room temperature measurement," Meas. Sci. Technol. **21**(2), 025310 (2010).
19. G. C. Bjorklund, "Frequency-modulation spectroscopy: a new method for measuring weak absorptions and dispersions," Opt. Lett. **5**(1), 15–17 (1980).
20. R. Slavík, J. Homola, and J. Ctyroky, "Single-mode optical fiber surface plasmon resonance sensor," Sens. Actuators, B **54**(1–2), 74–79 (1999).
21. A. Suzuki, J. Kondoh, Y. Matsui, S. Shiokawa, and K. Suzuki, "Development of novel optical waveguide surface plasmon resonance (SPR) sensor with dual light emitting diodes," Sens. Actuators, B **106**(1), 383–387 (2005).
22. A. Yalcin, K. C. Popat, J. C. Aldridge, T. A. Desai, J. Hryniewicz, N. Chbouki, B. E. Little, O. King, V. Van, S. Chu, D. Gill, M. Anthes-Washburn, M. S. Unlu, and B. B. Goldberg, "Optical sensing of biomolecules using microring resonators," IEEE J. Sel. Top. Quantum Electron. **12**(1), 148–155 (2006).
23. K. De Vos, I. Bartolozzi, E. Schacht, P. Bienstman, and R. Baets, "Silicon-on-Insulator microring resonator for sensitive and label-free biosensing," Opt. Express **15**(12), 7610–7615 (2007).
24. C. A. Barrios, K. B. Gylfason, B. Sánchez, A. Griol, H. Sohlström, M. Holgado, and R. Casquel, "Slot-waveguide biochemical sensor," Opt. Lett. **32**(21), 3080–3082 (2007).
25. P. Y. Li, B. Lin, J. Gerstenmaier, and B. T. Cunningham, "A new method for label-free imaging of biomolecular interactions," Sens. Actuators, B **99**(1), 6–13 (2004).
26. E. Chow, A. Grot, L. W. Mirkarimi, M. Sigalas, and G. Girolami, "Ultracompact biochemical sensor built with two-dimensional photonic crystal microcavity," Opt. Lett. **29**(10), 1093–1095 (2004).
27. L. Rindorf, J. B. Jensen, M. Dufva, L. H. Pedersen, P. E. Høiby, and O. Bang, "Photonic crystal fiber long-period gratings for biochemical sensing," Opt. Express **14**(18), 8224–8231 (2006).
28. Z. H. He, Y. N. Zhu, and H. Du, "Long-period gratings inscribed in air- and water-filled photonic crystal fiber for refractometric sensing of aqueous solution," Appl. Phys. Lett. **92**(4), 044105 (2008).
29. F. Tian, Z. He, and H. Du, "Numerical and experimental investigation of long-period gratings in photonic crystal fiber for refractive index sensing of gas media," Opt. Lett. **37**(3), 380–382 (2012).

1. Introduction

Because of their many advantages such as high sensitivity, low cost, small size, and multiplexing capability, refractive index (RI) sensors based on fiber Bragg grating (FBGs) are among the most-studied types of fiber-optic RI sensors [1–8]. Current FBG-based RI sensors are plagued by several drawbacks. In order for a FBG fabricated on regular solid fibers to perform RI sensing, the entire cladding of the fiber in the FBG region needs to be removed to expose the evanescent field into the surrounding environment. The thinned fiber region often has diameters <10 μm, compromising the mechanical strength and practical usefulness of the sensor. In addition, the FBG RI sensors are generally not compatible to microfluidic systems as they need to be immersed in the liquids to perform RI sensing, which requires a large amount of sample. Another drawback of FBG RI sensors is their large cross-sensitivity to temperature. Due to the thermo-optic effect of the fiber material, the Bragg wavelength of a FBG shifts as temperature changes with a sensitivity of ~9.8 pm/°C [7]. A promising method to compensate for the temperature cross-sensitivity is to use a FBG inscribed on an H-shaped fiber obtained by etching a side-hole fiber [4] or Panda fiber [9] from outside of the fiber with large fraction of the core energy leaking to the environment. RI sensing with temperature insensitivity can also be achieved by writing FBGs on rectangular microfibers [10]. Due to the large birefringence, the reflection spectrum of the FBG features two Bragg peaks, corresponding to the two polarization modes. RI sensing is achieved by measuring the spectral separation of the two peaks. Temperature can also be obtained from the shift of the individual peaks. However, due to the broad spectral feature of FBGs, the RI sensing resolution demonstrated in [4, 9] is rather limited. In addition, like etched FBGs, both the H-shaped fiber and the rectangular microfiber suffer from greatly reduced mechanical strength and microfluidic incompatibility.

Here, we present a novel fiber-optic RI sensor based on a high-Q π-phase-shifted FBG (πFBG) inscribed on a side-hole fiber. Similar to the H-shaped fiber, the temperature cross-sensitivity is reduced using the changes in the fiber birefringence caused by the circularly

#238231 Received 16 Apr 2015; revised 4 Jun 2015; accepted 14 Jun 2015; published 17 Jun 2015

non-symmetric interaction between the surrounding RI and the evanescent field of the core mode. However, the sensor reported here possesses several prominent advantages: 1) the spectral features of the high-Q πFBG for RI sensing are much narrower than those of regular FBGs (a few pm or less vs. >100 pm), resulting in improved spectral detection resolution over the sensor based on regular FBGs; 2) the outer diameter of the fiber is not reduced and the mechanical integrity of the sensor is not compromised; and 3) the sensor is inherently compatible to microfluidic systems as the holes naturally serve as microfluidic channels for convenient sample delivery with reduced sample amount. In addition, we demonstrate a novel demodulation method for such a sensor using a frequency-modulated narrow-linewidth laser source to significantly enhance the dynamic range of the sensor.

2. Sensor design and numerical simulation

The schematic of the RI sensor is shown in Fig. 1(a). It consists of a πFBG directly fabricated on a side-hole fiber. The two air-holes in the cladding run along the whole length of the fiber and naturally serve as microfluidic channels for convenient delivery of the liquid samples to the sensing area. The holes are very close to the fiber core so that the evanescent field of the core mode can interact with the liquids in the holes. Due to the spatial distribution of the holes, the birefringence of the fiber is dependent on the liquid RI. The πFBG has a π-phase shift at the center of an otherwise uniform grating structure. It can be conceptually considered as a Fabry-Perot cavity formed by two highly reflective FBG mirrors, resulting in two narrow notches in the reflection spectrum, each of which corresponds to a polarization state. The wavelength positions of the spectral notches are given by the Bragg wavelengths of $\lambda_x = 2n_x\Lambda$ and $\lambda_y = 2n_y\Lambda$, where Λ is the grating pitch and n_x and n_y are the effective RIs of the two polarization modes along the two principle axes (denoted as x- and y-axes). The fiber birefringence, and consequently the RI of the liquid in the holes, can be measured by the spacing of the two spectral notches, $\Delta\lambda = \lambda_x - \lambda_y$, as shown in Fig. 1(b). Again, because the spectral notches are extremely narrow (a few pm or less), their spectral separation and the liquid RI can be measured with high resolution. Moreover, as temperature variations cause almost identical changes to both n_x and n_y, the RI sensing has reduced cross-sensitivity to ambient temperature.

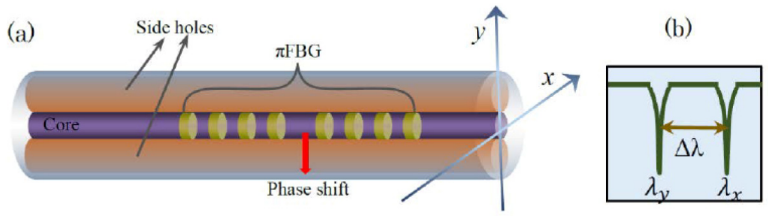

Fig. 1. (a) Schematics of the RI sensor structure and (b) its reflection spectrum.

Numerical simulations are performed to study the RI sensitivity. The side-hole fiber used in the simulation has the following parameters: core diameter = 5.90 μm; core RI = 1.4480; cladding RI = 1.4412; side-hole diameter = 40.6 μm; and distance between the centers of the two holes = 46.0 μm. The Bragg wavelength of the πFBG is assumed to be ~1550 nm. The diameters of the holes and distance between holes are selected to match the geometric parameters of the fiber used in the experiment. The effective RIs, n_x and n_y, and the mode field distribution of the polarization modes are calculated using COMSOL. Figure 2(a) shows the intensity distributions of the y-polarized mode when the RIs in the holes are 1 and 1.440. The field distribution for the case of air is obviously elliptical, indicating a large fiber birefringence; while the RI in the holes increase to 1.440, the field distribution becomes more

#238231 Received 16 Apr 2015; revised 4 Jun 2015; accepted 14 Jun 2015; published 17 Jun 2015

circularly symmetric, suggesting a reduced fiber birefringence. Figure 2(b) and 2(c) show, respectively, the spectral spacing of the two notches of the πFBG and the RI sensitivity (defined as the change in the spectral notch separation from unit RI change in the hole). Again it is shown that the spectral spacing nonlinearly reduces from ~300 pm when the holes are filled with air to 0 when the RI in the holes increases to approach the RI of the fiber cladding (RI = 1.440). The RI sensitivity has negative values as expected (decreased spacing with increasing RI) and the absolution values of the RI sensitivity increases exponentially as the RI in the holes increases.

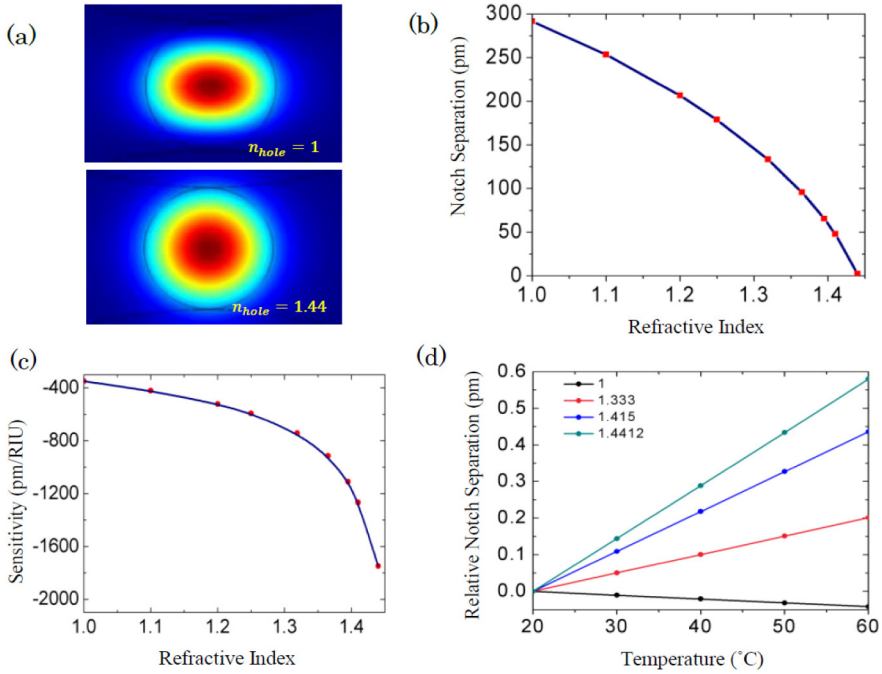

Fig. 2. (a) Intensity distribution of the y-polarized mode when the side holes of the fiber are filled with RIs of 1 and 1.44; (b) simulated spectral notch separation vs. RI in the holes; (c) RI sensitivity vs. RI in the holes; and (d) the sensor response to temperature when the side holes of the fiber are filled with different RIs.

The inherent temperature cross-sensitivity of the sensor, which is defined as the sensor response to a unit temperature change when the holes are filled with a material of constant RI, was also simulated on the side-hole fiber model whose geometry matches the one used in the experiment. Two contributing mechanisms are considered. The first is the thermo-optic effect of the fiber material. Assuming that the thermo-optic coefficients (TOCs) for both the cladding and the core of the fiber are 8.6×10^{-6}/°C [11], Fig. 2(d) shows the simulated relative spectral separation of the two notches as a function of temperature when the holes are filled with materials of different RIs. It is seen that temperature cross-sensitivity is highly dependent on the RI of the holes and, in general, the temperature sensitivity is larger when the holes RI is closer to the cladding RI. However, the simulated maximum temperature sensitivity is only 0.0145 pm/°C when the RI of the holes is equal to the cladding RI (1.4412). When the RI of the hole is 1.319 (RI of pure water at 1550 nm), the temperature sensitivity is reduced to ~0.005 pm/°C. The other mechanism, which is the fiber birefringence induced by the different thermal-expansion coefficients (TECs) of the fiber cladding and core, also plays an important role in the temperature sensitivity of the sensor. Assuming the fiber core is a silica glass doped with 4.5 mol.% GeO2, similar to a SMF-28 fiber, the TECs for the cladding and core are, respectively, 5.4×10^{-7}/°C and 8.3×10^{-7}/°C [12, 13]. Finite element (FE)

#238231 Received 16 Apr 2015; revised 4 Jun 2015; accepted 14 Jun 2015; published 17 Jun 2015

analysis is then performed using COMSOL to simulate changes in the strain field caused by temperature variations. To explain the non-uniformity of the train field induced by the non-symmetric structure and the differential thermal expansion between the core and cladding, Fig. 3(a) shows the cross-sectional distribution of the overall strain amplitude, $\sqrt{\varepsilon_{xx}^2+\varepsilon_{yy}^2}$, where ε_{xx} and ε_{yy} are the strain components along the two axial directions, caused by a temperature change from 20 to 1000 °C. The notch separation from strain is calculated according to [14]

$$\Delta\lambda = -n^3\left(p_{11}-p_{12}\right)\left(\varepsilon_{xx}-\varepsilon_{yy}\right)\Lambda, \tag{1}$$

where p_{ij} are the strain-optic coefficients of the fiber material, and n is the effective RI of the optical mode. For each of the strain components, its average value over the core area is used in Eq. (1). The simulation shows that the temperature sensitivity caused by thermal stress is –0.024 pm/°C. Noting that the simulated RI sensitivity around 1.319 (RI of pure water at 1550 nm) is ~736 pm/RIU, the sensor has a RI-to-temperature sensitivity ratio of 3.3×10^{-5} RIU/°C, which is lower than many RI sensors based on regular FBGs [3, 8]. Smaller temperature sensitivity can be achieved by using a fiber with a core and cladding of similar TECs [12].

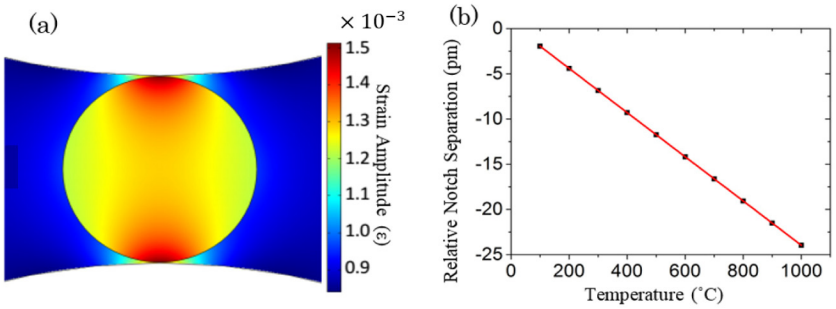

Fig. 3. (a) Simulated amplitude distribution of the strain field due to a temperature increase from 20 to 1000°C and (b) relative spectral notch separation as a function of temperature due to the different TECs between fiber core and cladding.

It is worth noting that, in practice, the RI of the liquid filling the holes likely change with temperature due to the thermo-optic effect. The refractometer will respond to these changes and its response is specific to the thermo-optic properties of the sample. Therefore, it is reasonable to assume a constant RI in the holes to numerically characterize the inherent temperature cross-sensitivity of the refractometer. In some applications, such as label-free biosensing, the sensor response to temperature induced RI changes of the sample may be undesirable. However, an inherently temperature-insensitive refractometer is important for many other applications where accurate measurement of sample RIs at different temperatures is required, such as thermo-optic characterization of liquid samples.

3. Sensor fabrication and characterization

The proposed RI sensor was experimentally demonstrated. A 7-mm long highly-reflective πFBG was written on a side-hole fiber using a 193 nm excimer laser and a phasemask on a nano-positioning stage, as described in [14]. The image on the left in Fig. 4(a) is the cross-sectional view of the side-hole fiber. These holes were enlarged to expose the core mode into the holes by chemically-etching the walls from inside the holes using buffered hydrofluoric acid (BHF). In order to monitor the grating reflection spectrum during the etching process, a

#238231 Received 16 Apr 2015; revised 4 Jun 2015; accepted 14 Jun 2015; published 17 Jun 2015

microfluidic system using the holes as the microfluidic channels, as shown in Fig. 4(b), was designed and fabricated. Specifically, a single-mode fiber (SMF) was spliced to the side-hole

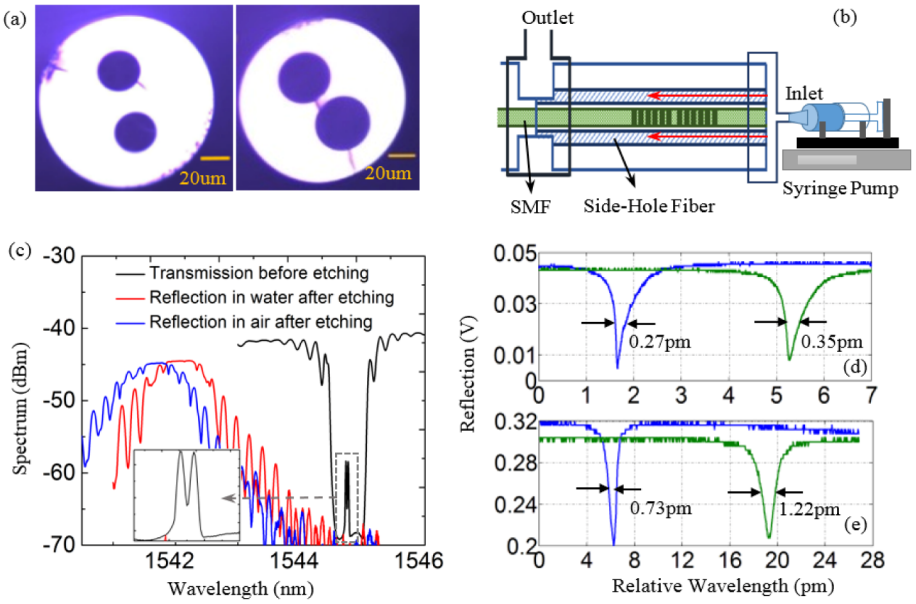

Fig. 4. (a) Cross-sectional view of the side-hole fiber before (left) and after (right) etching; (b) schematic of the sensor system with microfluidic capability; (c) spectrum of the πFBG before and after etching measured by OSA; (d) and (e): the two polarized spectral notches before (d) and after (e) etching.

fiber at one end and the holes of the side-hole fiber were opened to the environment at the splicing junction by BHF etching using the steps detailed in [15]. The BHF was injected to the holes from the free-end of the side-hole fiber using a microfluidic pump and the reflection spectrum was monitored from the SMF side using an unpolarized white-light source and an optical spectrum analyzer (OSA). This microfluidic system was also used later to deliver the fluidic samples to the sensing area for RI measurement. The etching process was stopped right before a significant amount of loss in the πFBG reflection was observed from the OSA. The image on the right in Fig. 4(a) is the cross-sectional view of the fiber after etching, indicating the edge-to-edge distance between the holes was reduced to ~7.2 μm. The dimensions of the etched holes can be precisely controlled by the BHF concentration, the flow rate, and the etching time. The transmission spectrum of the πFBG before fiber etching is shown as the black curve in Fig. 4(c). Due to the initial fiber birefringence, the transmission spectrum at the Bragg wavelength of πFBG shows two peaks separated by 25 pm, each of which corresponded to a polarization state, as shown in the inset to Fig. 4(c). The reflection spectra of the πFBG after etching when the holes were filled with air and water are shown as the blue and red curves, respectively, in Fig. 4(c). It is seen that the etching blue-shifted the center wavelength of the πFBG by 3.15 nm (from 1544.75 nm to 1541.60 nm) due to the reduced average RI in the cladding area. Filling the holes of the etched fiber with water caused a red-shift of ~0.5 nm. Due to the limited resolution of the OSA (20 pm), a tunable laser with a linewidth <300 kHz was used to measure the spectral width of each of the spectral notches by sweeping the laser wavelength. Figure 4(d) shows the measured spectral notches of the πFBG before fiber etching. It is seen that the 3-dB spectral widths of the notches at the longer wavelength and shorter wavelength were, respectively, 0.27 pm and 0.35 pm, corresponding to Q-factors of 5.7×10^6 and 4.4×10^6, respectively. These spectral notches after fiber etching are shown in Fig. 4(e). The etching process resulted in increased

#238231 Received 16 Apr 2015; revised 4 Jun 2015; accepted 14 Jun 2015; published 17 Jun 2015

roughness of the hole surface, leading to increased scattering loss to the core mode. As a result, the spectral widths of two πFBG notches were increased to 0.73 and 1.22 pm; accordingly their Q-factors were reduced to 2.1×10^6 and 0.74×10^6, respectively. It is also noticed that the notch depths and the optical power of the reflected signal were significantly reduced by the etching process. Nevertheless, the Q-factors are still higher than RI sensors based on regular FBGs by ~2 orders of magnitudes, resulting in significantly improved resolution in detecting the RI-induced spectral shift of the notches. The Q-factors of the sensors can be improved by more sophisticated etching processes that can lead to smoother fiber surface, such as BHF etching with ultrasonic agitation [16]. The etching also significantly increased the fiber birefringence. As shown later, after etching, the spectral separation was increased to ~370 pm when the holes were filled with air.

4. Experimental results

RI sensing is achieved by measuring the spectral spacing of the two notches. The spectral shifts of high-Q optical resonators are typically measured by a diode laser tuned by a piezoelectric transducer [17] or a distributed feedback semiconductor laser tuned by current injection [18]. Their tuning range is typically limited. For example, the fine-tuning range of the laser used in our experiment was 96 pm, which was insufficient for our πFBG sensor whose spectral spacing of the notches was up to 370 pm with air-filled holes. The dynamic range of the RI measurement is therefore limited to the wavelength tuning range of the laser source. We propose and demonstrate the use of laser frequency modulation (FM) [19] in the demodulation for enhanced sensor dynamic range. Figure 5(a) shows the schematics of the demodulation system, where a 10 GHz $LiNO_3$-based fiber-optic phase modulator driven by an amplified tunable RF source (HP-8684B) was included after the laser and a polarization controller (PC). The laser after the phase modulator was delivered to the πFBG sensor and the reflected light was directed to a photodetector through a circulator. Another PC was used before the sensor to ensure that the light into the sensor had both polarization components for simultaneous capture of the notches on the oscilloscope. The electric field intensity from a monochromatic laser at frequency of ω_0 can be written as $E(t) = E_0 \exp(i\omega_0 t)$, where E_0 is the field amplitude and t denotes time. After its phase is modulated by a sinusoidal function from the RF source through the phase modulator, the field becomes [11]

#238231 Received 16 Apr 2015; revised 4 Jun 2015; accepted 14 Jun 2015; published 17 Jun 2015

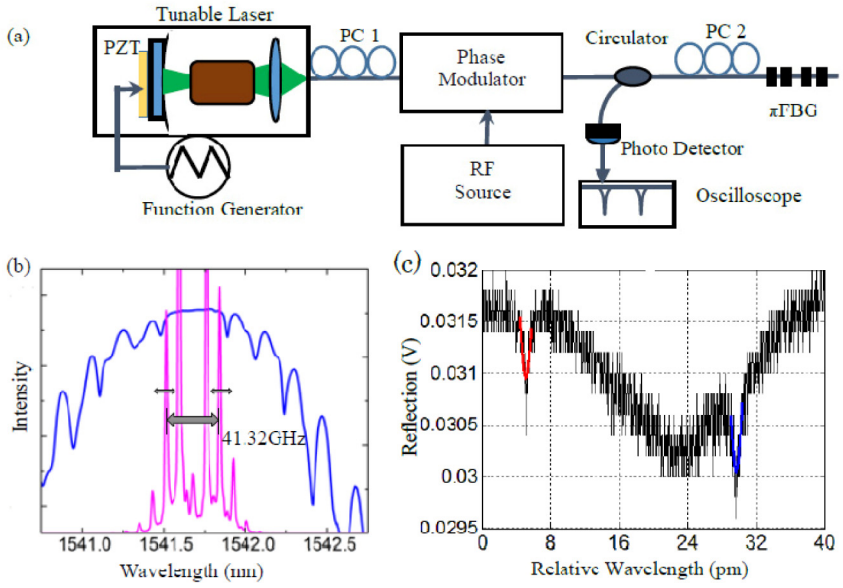

Fig. 5. (a) Schematic of the sensor demodulation system; (b) reflection spectrum of the sensor (blue, in logarithmic scale) and spectrum of the laser after FM (pink, in linear scale) measured by the OSA; and (c) spectrum of the two spectral notches shown on the oscilloscope.

$$E(t) = E_0 \exp\left[i\left(\omega_0 t + M \sin \omega_m t\right)\right] = E_0 \exp\left(i\omega_0 t\right) \sum_{n=-\infty}^{+\infty} J_n\left(M\right) \exp\left(in\omega_m t\right) \tag{2}$$

where ω_m is the frequency of the RF source, M is the modulation index determined by the RF power driving the phase modulator, and J_n is the n^{th}-order Bessel function of the first kind. It is seen that the FM laser beam has discrete, coherent, and equally-separated laser lines at $\omega_0 \pm n\omega_m$, whose relative intensities can be tuned to a limited extent by the RF power. Therefore, combining multiple laser lines, the tunable laser can be used to measure the spectral notch spacing much larger than the tuning range of each individual laser line. For example, in our experiment, in order to measure the spectral spacing of the πFBG notches when the holes were filled with air, we used a modulation frequency of >10 GHz and the modulation index was tuned so that a significant amount of the laser power was carried by the two second-order laser lines at $\omega_0 \pm 2\omega_m$. Figure 5(b) shows the FM laser spectrum measured by the OSA. For comparison, the reflection spectrum of the πFBG is also shown. Each of the two 2nd-order FM laser lines was close to one of the spectral notches. Therefore, both spectral notches were able to be simultaneously recorded by the oscilloscope using a very small wavelength-tuning range of the laser, as shown in Fig. 5(c). It is seen that a tuning range of 40 pm for the laser was sufficient to measure the spectral spacing of the πFBG notches that were more than 350 pm apart.

Using the demodulation method, RI measurement was conducted at 1.319 (RI of pure water at 1550 nm) region using ethanol/water solutions and at 1.396 (estimated RI of a 58 wt. % glycerine solution at 1550 nm) region using glycerine/water solutions. The RIs were varied around these values by slightly changing the solution concentrations. The solutions were delivered to the πFBG region using the microfluidic system shown in Fig. 3(c). Due to the microfluidic capability, the small size of the holes, and the short length of the πFBG, an amount of a few tens of μL sample was sufficient for each measurement. Figures 6(a) and

#238231 Received 16 Apr 2015; revised 4 Jun 2015; accepted 14 Jun 2015; published 17 Jun 2015

6(b) show the spectral spacing of the πFBG notches as a function of the liquid RI in the holes. The sensor response exhibits good linearity with RI sensitivities of −618 and −957 pm/RIU at RIs of 1.319 and 1.396, respectively. The experimental results for RI sensitivity agree relatively well with the theoretical results (−736 and −1122 pm/RIU at RIs of 1.319 and 1.396, respectively) shown in Fig. 2(c). As the fiber parameters of the core and cladding RIs and the core diameter were unknown, the relatively small discrepancies are believed to arise from the errors of these parameters used in the simulation.

As the sensor was damaged in our testing, a second sensor was fabricated to study the RI resolution and temperature cross-sensitivity. For the characterization of RI resolution, the notch spacing of the sensor (~370 pm) was continuously measured when the holes were filled with air. For the FM demodulation, the RF frequency was set to 11.21 GHz and the ± 2nd-order components were used. The measured notch separation as a function of time is shown in Fig. 6(c). The standard-deviation of the measured notch spacing is 0.033 pm, corresponding to a RI measurement resolution of 5.3×10^{-5} RIU using the RI sensitivity of −618 pm/RIU at RI = 1.319 obtained for the first sensor. During the experiment, we note that the spacing measurement is sensitive to the polarization state of the laser. We believe that the fluctuations of the measured notch separation arose primarily from the changes in the polarization state due to temperature variations or fiber bending. However, this polarization-induced fluctuation could be reduced by a polarization scrambler placed in front of the πFBG that randomizes the polarization states.

It is worth pointing out that the RI sensitivity of many other optical RI sensor platforms, such as those based on waveguide surface Plasmon resonator [20, 21], ring resonators [22–24], photonic crystals [25, 26], and long period gratings (LPGs) [27–29], have demonstrated much higher RI sensitivity. However, the RI resolution is of more importance in practical applications. Due to the high Q-factor that leads to a high spectral resolution, the refractometer demonstrated here, despite having a medium RI sensitivity, achieves a RI sensing resolution that is comparable to most of the above sensors.

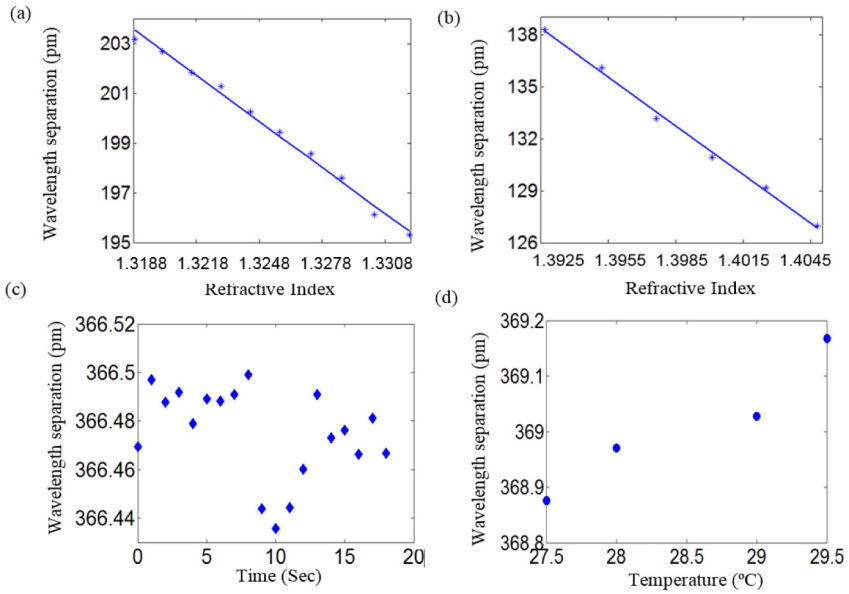

Fig. 6. Sensor responses to RI at RIs around 1.319 (a) and around 1.396 (b); spectral notch separation vs. time (c) and spectral notch separation vs. temperature (d).

Finally, the temperature cross-sensitivity was tested by heating the sensor in a temperature chamber and measuring the notch spacing as the sensor cooled down. The result, shown in

#238231 Received 16 Apr 2015; revised 4 Jun 2015; accepted 14 Jun 2015; published 17 Jun 2015

Fig. 6(d), indicates a temperature sensitivity of 0.15 pm/°C, which is 65 times smaller than a regular FBG. We note that, compared to the simulation result shown in Fig. 3(b), the measured temperature cross-sensitivity has much larger absolute values. As discussed above, the temperature-induced polarization change is believed to be responsible for the relatively large variations of the measured spectral notch spacing in the experiment, which completely masked the small inherent temperature sensitivity of the sensor.

5. Summary

In summary, we present a novel fiber-optic RI sensor based on a πFBG written on a side-hole fiber. The reflection spectrum of the πFBG exhibits two narrow spectral notches related to the fiber birefringence and their spacing is sensitive to the RI in the holes with little cross-sensitivity to temperature. The outer diameter of the fiber is not reduced to retain the mechanical strength of sensor. The side-hole fiber is naturally integrated into a microfluidic system where the holes in the fiber serve as microfluidic channels through which liquid samples of small amount are conveniently delivered to the sensing area. A novel demodulation method based on laser FM is demonstrated that allows measuring large spectral spacing using a laser with small wavelength fine-tuning range. A πFBG sensor with Q-factors of 2.1×10^6 and 0.74×10^6 for the two spectral notches is fabricated and tested for RI measurement with a RI sensitivity of −618 pm/RIU at the RI of 1.319. The spectral resolution and temperature cross-sensitivity are also experimentally studied for such sensors.

Acknowledgments

This work was supported by the U.S. National Science Foundation under grant no. EPS-1004094 and U.S. Office of Naval Research under grant no. N000141110705.

#238231 Received 16 Apr 2015; revised 4 Jun 2015; accepted 14 Jun 2015; published 17 Jun 2015